Isotropic 3D topological phases with broken time reversal symmetry

Hélène Spring[1], Anton R. Akhmerov[1], Dániel Varjas[2,3,4,5*]

1 Kavli Institute of Nanoscience, Delft University of Technology, P.O. Box 4056, 2600 GA Delft, The Netherlands
2 Department of Physics, Stockholm University, AlbaNova University Center, 106 91 Stockholm, Sweden
3 Max Planck Institute for the Physics of Complex Systems, Nöthnitzer Strasse 38, 01187 Dresden, Germany
4 IFW Dresden and Würzburg-Dresden Cluster of Excellence ct.qmat, Helmholtzstr. 20, 01069 Dresden, Germany
5 Department of Theoretical Physics, Institute of Physics, Budapest University of Technology and Economics, Műegyetem rkp. 3., 1111 Budapest, Hungary
*varjas.daniel@ttk.bme.hu

Abstract

Axial vectors, such as current or magnetization, are commonly used order parameters in time-reversal symmetry breaking systems. These vectors also break isotropy in three dimensional systems, lowering the spatial symmetry. We demonstrate that it is possible to construct a fully isotropic and inversion-symmetric three-dimensional medium where time-reversal symmetry is systematically broken. We devise a model of an amorphous material with scalar time-reversal symmetry breaking, implemented by hopping through chiral magnetic clusters along the bonds. The presence of only average spatial symmetries—continuous rotation and inversion—is sufficient to protect a topological phase, yielding a statistical topological insulator. We demonstrate the topological nature of our model by constructing a bulk integer topological invariant, which guarantees gapless surface spectrum on any surface with an odd number of Dirac nodes, analogous to crystalline mirror Chern insulators. We also show the expected transport properties of a three-dimensional statistical topological insulator, which remains critical on the surface for odd values of the invariant.

1 Introduction

A three-dimensional (3D) isotropic medium has the highest degree of spatial symmetry. Unless they are explicitly broken, non-spatial symmetries like time-reversal symmetry (TRS) are also present in isotropic systems. Removing TRS typically also breaks isotropy, for example ferromagnets break TRS but also break rotation symmetry along the axes which are not parallel to the magnetization. Antiferromagnets restore some spatial symmetries such as the product of inversion and TRS, but also break rotation symmetry [1]. The spatial symmetries are partially restored in altermagnets [2]—a recently proposed class of materials combining lack of net magnetization with a spin splitting away from away from high-symmetry momenta, however even in these materials the magnetic order is incompatible with full isotropy.

The spatial symmetries of a system are relevant both for defining and protecting topological phases [3–6]. While initially considered to be susceptible to disorder, topological systems relying on spatial symmetries were later shown to be protected from localization as long as the disordered ensemble respects the spatial symmetries [7–9]. This protection by an 'average' symmetry, a hallmark of statistical topological insulators, is especially powerful in isotropic amorphous media. In an earlier work we demonstrated that unlike their crystalline counterparts—where the spatial symmetry is only preserved by certain crystal terminations—it is possible to utilize the isotropy of a 2D amorphous medium to extend the topological protection to any edge of the system [10].

Motivated by the two above considerations, we ask whether it is possible to find a model hosting a topological phase protected only by average continuous spatial symmetries. Because both TRS and average TRS protect topological phases, we additionally require that the desired model also breaks TRS on average. By designing a scalar, rather than a vector TRS breaking order using a random assembly of chiral magnetic molecules, we answer positively to the above question. Specifically we demonstrate that the average spatial symmetries present in 3D isotropic media protect topological phases even when TRS is systematically broken, and that the amorphous realization of such a system is a statistical topological insulator. This topological phase is analogous to crystalline mirror-Chern insulators, except that the isotropic system hosts gapless modes on any flat surface regardless of orientation. Furthermore, we identify a bulk higher-order electromagnetic response which distinguishes isotropic media with or without scalar TRS breaking.

The organization of the manuscript is as follows. In Sec. 2.1 we formulate an isotropic continuum model where TRS is systematically broken. We present a microscopic Hamiltonian originating from an amorphous network of chiral magnetic molecules that replicates this model. In Sec. 2.2 we demonstrate the topological nature of our model by formulating bulk invariants, examining surface dispersions, and analyzing transport of the topologically protected surface modes. As established in the study of statistical topological insulator phases, we show that the model localizes when its degrees of freedom are doubled. We conclude in Sec. 3.

2 Results

2.1 Symmetry analysis

2.1.1 Continuum model

In order to guide the construction of a microscopic model, we begin with developing a minimal continuum ($\boldsymbol{k}\cdot\boldsymbol{p}$) model respecting the desired symmetries. We follow the procedure outlined in Ref. [10]: We start by generating a minimal 2D Dirac Hamiltonian. The mass terms present in this minimal Hamiltonian are capable of gapping out the spectrum. We then search for all of the symmetry representations of inversion and continuous rotation symmetry that remove the mass terms of the minimal Hamiltonian, thereby ensuring that the spatial symmetries prevent a gap from opening. These 2D Hamiltonians correspond to the surfaces of 3D topological bulk models in the same symmetry class. By utilizing the isotropy, we extend the symmetry representations from 2D to 3D to obtain the 3D bulk phases. We automate this process using the software package Qsymm [11]. The symmetry representations of the spatial symmetries are listed in App. A, Eq. (A.1) and (A.2). The resulting k-space model is of the form:

$$\begin{aligned} H_{4\times4}(\boldsymbol{k}) = (\mu_1 + t_2k^2)\sigma_0(\tau_0+\tau_z)/2 + (\mu_2+t_3k^2)\sigma_0(\tau_0-\tau_z)/2 \\ + (-t_1+t_4k^2)\boldsymbol{\sigma}\cdot\boldsymbol{k}\tau_y + (-t_0+t_5k^2)\boldsymbol{\sigma}\cdot\boldsymbol{k}\tau_x, \end{aligned} \tag{1}$$

where μ_i are chemical potential terms, t_i are the hopping terms, σ and τ are the Pauli matrices, with τ representing the orbital space ($\tau_z = \pm1$ corresponding to s and $p_{1/2}$ orbitals respectively) and σ representing spin space, $\boldsymbol{k} = (k_x, k_y, k_z)$, and $k^2 = \boldsymbol{k}\cdot\boldsymbol{k}$.

Limiting the model to terms quadratic in k means a parameter-dependent transformation of the form $\exp(i\tau_z\phi)$ is capable of removing the relative hopping phases between the s and $p_{1/2}$ orbitals (appearing as terms proportional to $\tau_{x/y}$) and restoring a TRS-like symmetry. Therefore, the model includes terms up to k^3 in order to remove this residual symmetry. A tight-binding model reproducing such features must include s—p hoppings with spin-orbit coupling and a distance-dependent complex phase.

Despite lacking TRS, the high degree of spatial symmetry of this model protects the twofold spin degeneracy of all bands. For a fixed $\boldsymbol{k}$, the eigenstates of (1) are eigenstates of the angular momentum operator in the direction parallel to $\boldsymbol{k}$. Mirror symmetry exchanges states with opposite angular momentum, thereby ensuring the degeneracy of the spin bands.

2.1.2 Microscopic implementation

Based on the symmetry-allowed terms of the continuum model (1), we now construct a microscopic model that preserves isotropy while breaking TRS. The minimal model contains two orbitals that have opposite inversion eigenvalues, which we choose as an s and a p orbital. We choose the $\boldsymbol{\sigma}$ degree of freedom to correspond to the electron spin, which makes the last four terms of Eq. (1) spin-orbit-like, although with an additional k-dependent phase shift necessary to break TRS. In order to realize these spin-orbit-like hoppings in a microscopic model, we therefore consider two separate atoms that host spinful s and $p_{x,y,z}$ orbitals respectively, as illustrated in Fig. 1(a). For the purpose of obtaining a minimal model, we separate the p orbitals into $p_{3/2}$ and $p_{1/2}$ orbitals with an atomic spin-orbit coupling, and consider only the lower-energy $p_{1/2,\uparrow\downarrow}$ subspace.

In order to break TRS, we introduce magnetic atoms between the s and p orbitals, a plausible setup in an amorphous structure formed form chiral magnetic molecules. Hopping between the two atoms occurs through a virtual process via four s orbitals on a plane perpendicular to the s–p bond axis, located on the middle of the bond [Fig. 1(a)]. These intermediate s orbitals each host a magnetic moment, such that together they form a chiral magnetic texture in the plane that contains them. The curl of the magnetic texture defines a TRS-odd vector, that combined with the hopping vector $\boldsymbol{r}$, defines a scalar quantity $(\boldsymbol{\nabla}\times\boldsymbol{M})\cdot\boldsymbol{r}$. This is the desired source of scalar TRS breaking. Tiling the space with such s–p bonds restores spatial symmetries, while keeping TRS broken. We will return to the question of how such background magnetic texture may arise at the end of this section.

The Hamiltonian of an x-aligned s–p bond is:

$$\begin{aligned} H_m = E_s\sum_{\sigma}|s_\sigma\rangle\langle s_\sigma| + E_p\sum_{i,\sigma}|p_{i\sigma}\rangle\langle p_{i\sigma}| + \sum_{n,\sigma}(\Delta|s_{n\sigma}\rangle\langle s_{n\sigma}| + t_s|s_\sigma\rangle\langle s_{n\sigma}| + \text{h.c.}) \\ + \sum_{i,n,\sigma}(t_{in}|p_{i\sigma}\rangle\langle s_{n\sigma}| + \text{h.c.}) + \alpha\hat{\boldsymbol{L}}_p\cdot\hat{\boldsymbol{\sigma}}_p + \sum_n \boldsymbol{B}_n\cdot\hat{\boldsymbol{\sigma}}_n, \end{aligned} \tag{2}$$

where $\sigma\in\{\uparrow,\downarrow\}$, $i\in\{x,y,z\}$, $n\in\{1,2,3,4\}$, $|s_\sigma\rangle$ are the spinful s orbital states, $|s_{n\sigma}\rangle$ are the mid-bond magnetic s_n orbitals, $|p_{i\sigma}\rangle$ are the $p_{x,y,z}$ orbitals, $E_{s/p}$ are the onsite

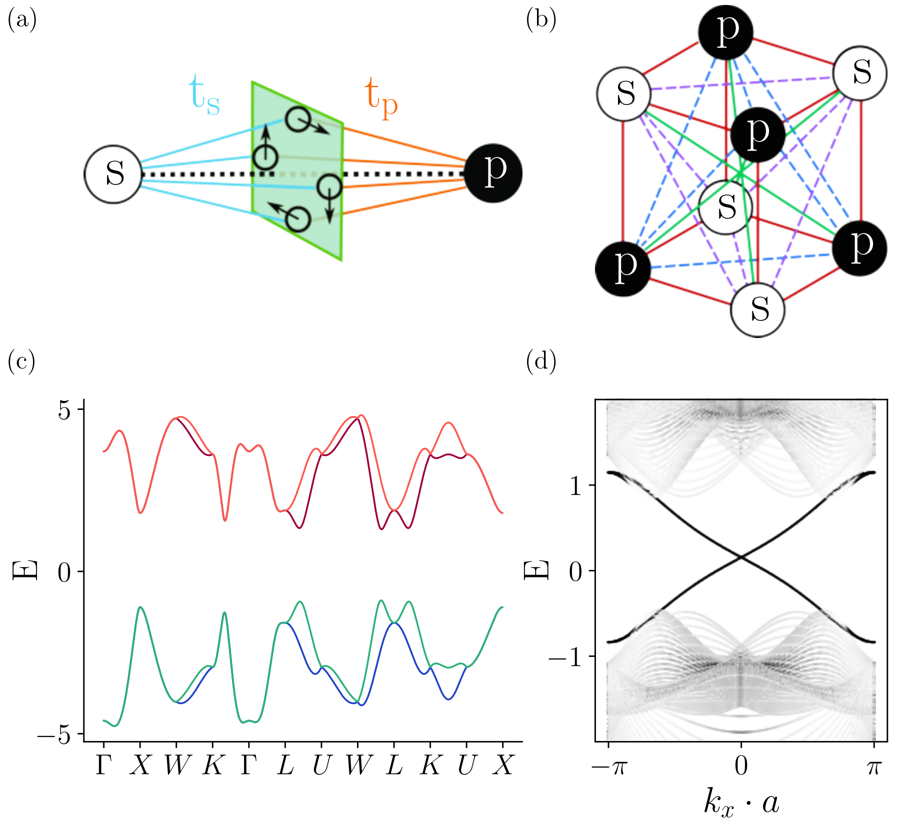

Figure 1: Time-reversal symmetry breaking in a microscopic system with inversion and rotation symmetry. (a) A bond between s and p orbitals hosting four mid-bond s orbitals (on plane shown in green) that host magnetic moments. (b) A section of a rock salt crystal structure made from the bond shown in (a). Red lines indicate nearest-neighbor hopping between s and p orbitals, dashed lines indicate next-nearest neighbor hopping between s (purple) and p (blue) orbitals, green lines indicate next-next-nearest neighbor hopping between s and p orbitals. (c) The bulk dispersion relation obtained from the crystal structure shown in (b) along the high-symmetry points of the face-centered cubic Brillouin zone. Different colors indicate different bands. (d) Bulk and surface dispersion of a 3D slab of the crystal. Darker color indicates a larger participation ratio. Plot details are in App. B.

energies of the s and p orbitals, Δ is the onsite energy of the mid-bond s_n orbitals, α is the magnitude of the atomic spin-orbit coupling splitting on the p orbitals, $\hat{\boldsymbol{\sigma}}_{p/n}$ are the spin operators on the p and s_n orbitals, $\hat{\boldsymbol{L}}_p$ are the orbital angular momentum operators on the p-orbitals, $\boldsymbol{B}_n$ are the magnetic moments of the s_n orbitals. Finally, t_{in} are the amplitudes of the s_n–p_i hopping, determined by whether the hopping between the $p_{x,y,z}$ orbitals and the s_n orbitals takes place via the positive or negative lobes of the p orbitals:

$$t_{in} = t_x \delta_{ix} + t_{yz}\delta_{iy}\mathrm{sgn}(y_n) + t_{yz}\delta_{iz}\mathrm{sgn}(z_n) \tag{3}$$

where y_n and z_n are the y and z coordinates of the s_n orbitals and $\mathrm{sgn}(0) = 0$.

We use second-order quasi-degenerate perturbation theory (assisted by the Python software package Pymablock [12]) to obtain the effective hopping t_{sp} between the s and $p_{1/2}$ orbitals. We find that the resulting terms have the desired symmetries by substituting in arbitrary parameters. We demonstrate this result in a limiting case defined by the set of inequalities $\alpha \gg \Delta + B \gg \Delta - B \gg E_s,\ E_p - \alpha,\ t_s,\ t_{x/y/z}$, which holds when spin-orbit coupling is large, and hopping only occurs via the lower-energy virtual level $\Delta - B$. The resulting expression for the effective hopping amplitude is:

$$t_{sp} = \frac{t_s(2t_x - it_{yz})}{\sqrt{3}(\Delta - B)} i\sigma_x. \tag{4}$$

This hopping has a complex hopping phase, which breaks TRS. The hopping phase is distance dependent due to the different distance dependence of the microscopic hopping amplitudes from the p_x and $p_{y,z}$ orbitals. This ensures that the hopping phase cannot be removed by a global basis-transformation introducing a relative phase between the s and p wavefunctions, resulting in an effective time-reversal symmetry. Hopping terms along directions other than x follow from applying rotation operators, resulting in hopping terms of the form $H^{\text{hopping}}_{s-p}(\boldsymbol{d}) = f\left(|\boldsymbol{d}|\right) \boldsymbol{d}\cdot\boldsymbol{\sigma}$ where $\boldsymbol{d}$ is the hopping vector, and f is a complex function of the hopping distance.

To demonstrate scalar TRS-breaking, we calculate the dispersion of a cubic rocksalt crystal endowed with this hopping term on the nearest neighbour and next-next-nearest neighbor s—p bonds [Fig. 1(b), for details see App. D]. The dispersion relation shows that the spin bands are split away from high-symmetry points and lines, demonstrating that TRS is systematically broken, while all space-group symmetries are preserved [Fig. 1(c)]. The surface dispersion shows gapless, propagating surface modes within the bulk gap, consistent with a crystalline mirror-Chern insulator state [Fig. 1(d)].

Lastly, we provide a minimal spin model that realizes the magnetic texture that we postulated. We assume that the magnetic moments on the mid-bond plane experience a strong easy-axis anisotropy, forcing them in the tangential direction around the bond axis. If we also include Dzyaloshinskii–Moriya interaction between neighbouring magnetic moments, this will favour perpendicular alignment, resulting in the type of chiral ground state we postulated. In fact, the number of mid-bond spins is not an essential ingredient of our construction, and with 3 spins in a triangle formation an antiferromagnetic, or with more than 4 symmetrically placed spins a ferromagnetic interaction would also result in a chiral state. This local magnetic interaction has a twofold degenerate ground-state, corresponding to opposite values of the scalar TRS-breaking order parameter. Including an antiferromagnetic coupling between nearby magnetic moments on neighbouring bonds favours the same chirality, resulting in a global ground state with a definite value of the scalar order parameter.

2.1.3 Amorphous realization

Amorphous systems possess average continuous rotation symmetry, average reflection and average inversion [10]. Since the scalar TRS-breaking mechanism is independent of bond orientation, an amorphous system endowed with this hopping possesses ensemble isotropy while also systematically breaking time-reversal.

We construct short-range correlated amorphous structures using the same procedure as in Ref. [10], treating system sites as hard spheres. The amorphous tight-binding Hamiltonian has the form

$$H = \sum_{\boldsymbol{r},i,j} H^{\text{onsite}}_{ij} c^\dagger_{\boldsymbol{r},i} c_{\boldsymbol{r},j} + \sum_{\langle \boldsymbol{r},\boldsymbol{r}'\rangle,i,j} H^{\text{hopping}}_{ij}(\boldsymbol{r}-\boldsymbol{r}') c^\dagger_{\boldsymbol{r},i} c_{\boldsymbol{r}',j}, \tag{5}$$

where the sums run over sites $\boldsymbol{r}$ and bonds $\langle \boldsymbol{r},\boldsymbol{r}'\rangle$ in the system, and on-site (spin and orbital) degrees of freedom i and j. The assumption of spatial isotropy constrains the dependence of H^{hopping} on the hopping vector, satisfied for example by H^{hopping}_{s-p} found in the previous section.

Rather than simulating an amorphous system with two families of atoms and two degrees of freedom per atom, for simplicity and without loss of generality we simulate one type of atom with four degrees of freedom. To further examine the extent of topological protection, we also define a model with twice the degrees of freedom and two protected Dirac cones on the surface in the continuum limit. We systematically find minimal real-space models of the form (5) compatible with full spatial isotropy using Qsymm, see App. A for the full definition of both models. We examine the spectral functions of the minimal model, and confirm the joint presence of a spectral gap and the lack of spin splitting [Fig. 2(a)], as expected from the symmetry analysis of the continuum model. The surface spectral function confirms the presence of gapless surface modes within the bulk gap [Fig. 2(b)].

2.2 Topological properties

2.2.1 Bulk invariants

To define the topological invariants, we observe that the high spatial symmetry guarantees that the protected band gap closings only occur at high symmetry momenta: $\boldsymbol{k} = \boldsymbol{0}$ and $\boldsymbol{k} = \boldsymbol{\infty}$ for the amorphous system. To compute the k-space topological invariant we use an effective k-space Hamiltonian H_{eff} that we obtain by inverting the single-particle Green's function that we project onto the plane wave basis, as described in Refs. [6, 10, 13, 14].

The invariants of 3D statistical topological insulators are constructed from the invariants of 2D strong topological phases [9]. The invariant of 2D class A systems is the Chern number, given by the integral of the Berry curvature over the 2D Brillouin zone at the Fermi energy. Our 3D class A model relies on mirror symmetry to protect its surface modes. Therefore a possible bulk invariant of this model is a mirror Chern number, given by the difference in Chern numbers of opposite mirror sectors:

$$C_M = \frac{1}{2}(C_+ - C_-), \quad C_\pm = \oiint \mathcal{F}_\pm(\boldsymbol{k}) d^2\boldsymbol{k}, \tag{6}$$

where the integral runs over a compactified mirror-invariant plane $\mathbb{R}^2 \cup \{\infty\}$ [10, 13] (e.g. $k_z = 0$, invariant under the mirror operator $k_z \to -k_z$ with $U_{M_z} = \mathcal{I}\exp(i\pi S_z)$), and $\mathcal{F}_\pm$ is the Berry curvature of the even/odd ($\pm i$ eigenvalue) mirror sub-blocks of the Hamiltonian. The invariant for crystal systems has the same form for a mirror-invariant plane in the crystal Brillouin zone [3]. However, because both the systems have inversion and rotation symmetries, the mirror Chern number can also be expressed in terms of rotation and inversion eigenvalues at high-symmetry momenta. Numerical results and a further discussion of invariants of the amorphous system are found in App. E.

2.2.2 Surface spectrum

As demonstrated in Fig. 1(d) for the crystalline system, the high-symmetry surface of the $C_M = 1$ model hosts a single Dirac cone, and multiple Dirac cones remain protected for $C_M > 1$. We expect that the high degree of ensemble averaged spatial symmetry of the amorphous Hamiltonian prevents surface states from being gapped out on any surface both for the single and doubled model ($C_M = 1$ and 2 respectively). We confirm this by numerically computing the surface spectral function

$$A(E, \boldsymbol{k}) = \sum_l \langle \boldsymbol{k}, l| \, \delta(H - E) \, |\boldsymbol{k}, l\rangle \,, \tag{7}$$

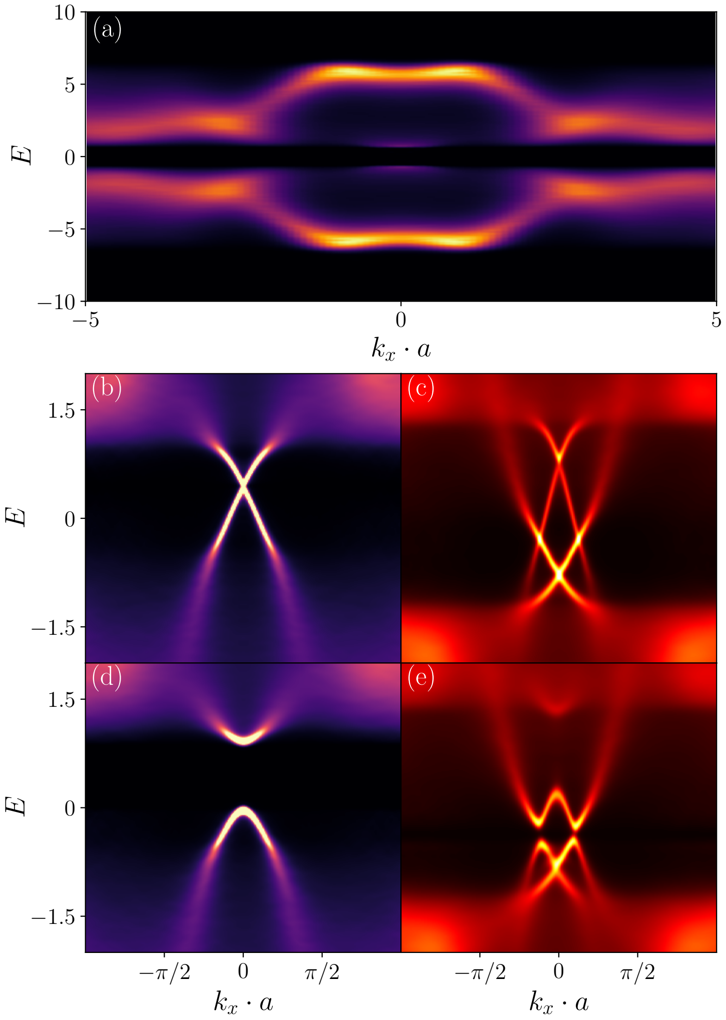

Figure 2: The (a) bulk and (b)-(e) surface spectral functions of the amorphous models. (b)-(c) The surface spectral functions of the single Dirac cone model (A.4) and the double Dirac cone model (A.8). (d)-(e) the same models as (b)-(c) but with broken spatial (mirror and rotation) symmetries. Plot details are in App. B.

using the Kernel polynomial method [10, 15, 16]. Here H is the real-space Hamiltonian of a finite slab, l runs over the internal degrees of freedom, and $|\boldsymbol{k}, l\rangle$ is a plane-wave state localized on one surface.

We find that both the original and doubled amorphous models have a nonzero surface density of states in the bulk gap, with one or two Dirac nodes located at zero momentum. [Fig. 2(b,c)]. This is a consequence of the nontrivial topology of the continuum system described by the bulk effective Hamiltonian. The surface spectral function in the k_x direction probes the topology of the $k_y = 0$ cut of the bulk effective Hamiltonian, which is invariant under M_y in the thermodynamic limit. This allows decomposition into two mirror sectors, each of which is a Chern insulator, resulting in an edge spectrum with C_M pairs of counter-propagating chiral edge states crossing the bulk gap. The modes with different chirality correspond to different mirror sectors, hence they are protected from gapping out by mirror-symmetric terms in the continuum model. We demonstrate that the surface states gap out when the symmetries protecting the topological phase (rotations and mirrors normal to the surface) are broken on average [Fig. 2(d,e)]. It is not clear, however, whether disorder that respects the mirror symmetry on average is capable of opening a spectral gap in the amorphous system with even C_M. The transport calculations in the next section show that the surface of the even phase localizes, which suggests that a local surface perturbation compatible with the average symmetry is capable of opening a spectral gap.

2.2.3 Surface transport

Reference [9] conjectures that only the $\mathbb{Z}_2$ part of the invariant provides topological protection, or in other words, that only the surface states of systems with odd C_M are protected from localization. In a crystalline system, the surface has an ensemble point group symmetry, and its localization properties are therefore equivalent to a doubled Chalker-Coddington network model, which has a localized phase with an anomalously large localization length [17, 18]. The conjecture, however, was not confirmed for 3D phases with continuous rotation symmetries, such as our amorphous model. To confirm the conjecture, we simulate the surface transport properties using amorphous network models.

We first simulate the transport properties of the regular network model as a baseline for the comparison. In the presence of disorder that preserves the spatial symmetries on average, the surface of the crystalline phase is equivalent to a critical Chern insulator. We simulate its transport properties with the Chalker-Coddington network model on the square lattice [19]. We fix the aspect ratio of the network to 1 and impose periodic boundary conditions along the y direction [Fig. 3(a)]. The scattering matrices at each node of the network are random 2×2 matrices sampled from a Haar-distributed $U(2)$ ensemble. The conductance through the system is:

$$G = \frac{e^2}{h} \sum_i T_i, \tag{8}$$

where T_i are the transmission probabilities from the modes entering one side of the network to the modes exiting on the other side. Since the aspect ratio equals to 1, the system conductivity $g = G$. We calculate the average conductivity $\langle g \rangle$ as a function of system size L and reproduce the known result $\langle g \rangle \approx 0.5$–$0.6 e^2/\hbar$ [20] [Fig. 3(d)], with the slow increase as a function of L due to finite-size effects. We investigate the localization properties of the double Dirac cone model by doubling the number of modes on each link, as shown schematically in Fig. 3(c). This system is expected to localize, based on both numerical [17] and analytical [18] studies. We draw the 4×4 scattering matrices of the doubled networks from the circular unitary ensemble and confirm localization at system sizes of several thousand sites [Fig. 3(d)].

We now simulate the conductance of our amorphous model, in order to determine whether the average continuous rotation symmetry has an effect on the conductance properties of the system. We define an amorphous 2D network model in order to simulate the average rotation symmetry using a fourfold coordinated random graph [13, 21], for details of the construction of the amorphous network see App. F. We use an annulus geometry in order to avoid issues constructing the network with periodic boundary conditions, and numerically calculate the conductance through the bulk from the modes entering the outer edge to the modes exiting the inner edge of the annulus [Fig. 3(b)]. The conductance G is calculated using (8), and the conductivity of the annulus equals:

$$g = \frac{1}{2\pi} G \log\left(\frac{R}{r}\right), \tag{9}$$

where R and r are the outer and inner radii of the annulus respectively. The results for the amorphous network closely follow the results for the regular network: the single

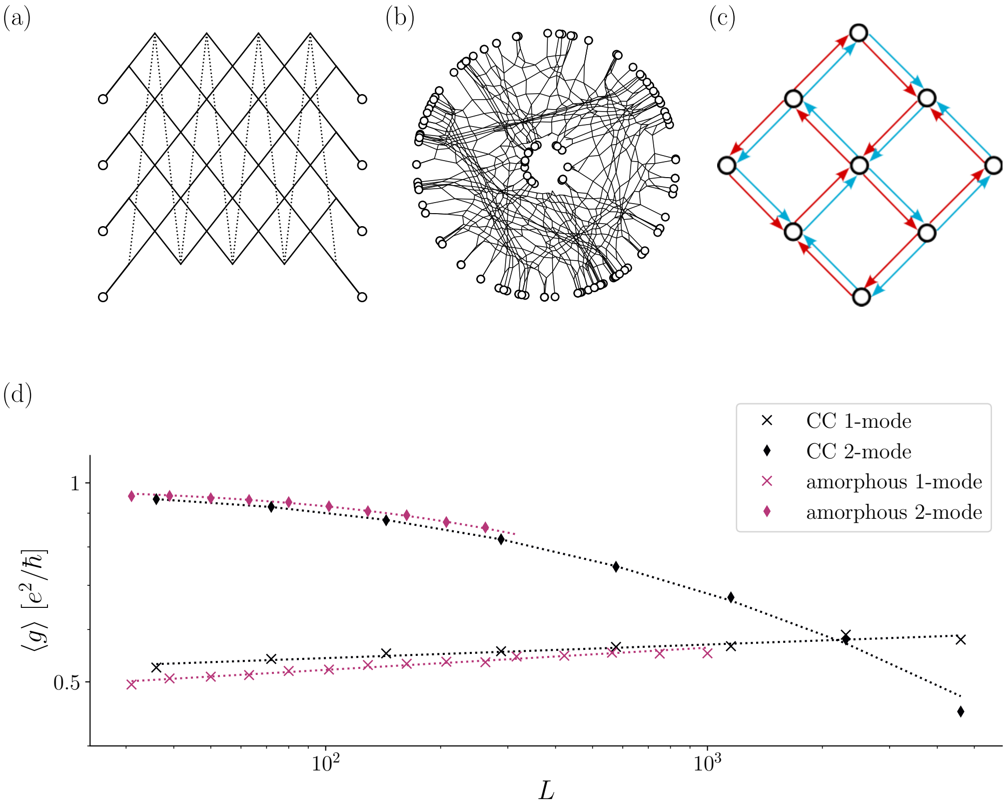

Figure 3: Conductivity of translationally invariant and amorphous networks. (a) Schematic of the Chalker-Coddington model. Dashed links loop in the vertical direction to indicate periodic boundary conditions. Circular nodes indicate external nodes where modes enter and exit the network. Internal nodes are located at all solid line crossings. (b) Schematic of the amorphous network. Circular nodes indicate external nodes where modes enter and exit the network. Nodes internal to the network are located at all line crossings. (c) Schematic of modes in the doubled model. (d) Average conductivity of the networks as a function of network length and width L and fits (dashed lines). Results are shown for the Chalker-Coddington (CC) network and amorphous network, with 1 mode per link (crosses) and 2 modes per link (diamonds). Plot details are in App. B.

Dirac cone conductivity falls within the $0.5 - 0.6e^2/\hbar$ range for small L and increases due to finite-size effects, and the double Dirac cone network localizes [Fig. 3(d)]. These observations confirm that a doubled phase transition is not protected from localization, even in the presence of average isotropy.

3 Discussion

In this work, we found that 3D isotropic systems breaking all non-spatial symmetries host topologically protected phases of matter. We devised a rotation- and inversion-symmetric continuum model with broken time-reversal symmetry, and presented a microscopic realization of this model in amorphous matter with average isotropy. The feasibility of amorphous magnetic structures assembled from chiral magnetic molecules or nanoparticles [22] is supported by experimental studies on Prussian blue analogues [23–25] and single-molecule magnets [26, 27], exhibiting magnetic interactions leading to ferrimagnetic and non-collinear antiferromagnetic ordering. We constructed a bulk $\mathbb{Z}$ invariant—expressible both in terms of symmetry eigenvalues and mirror Chern numbers— indicating the presence of a protected ungappable surface Dirac cone for odd values, which we numerically demonstrated.

We simulated the transport of our models using both regular and amorphous network models with random scattering at each node. We found results consistent with critical scaling, deviations from which are likely due to finite-size effects. Upon doubling the degrees of freedom in both the regular and amorphous networks, the modes localize as conjectured in Refs. [9, 17, 18]. Even though the numerics does not indicate a spectral gap forming for any higher number of surface Dirac cones, we expect that only an odd number are protected from localization and gapping out. We leave further investigation of the surface spectral properties in the even phases to future work.

Due to the combination of average continuous rotation symmetry and inversion symmetry, the spin bands in the bulk of the amorphous system are doubly degenerate. This raises the question whether the systematic breaking of TRS leads to a macroscopic change in the material properties. Enumerating the possible non-dissipative electromagnetic responses compatible with isotropy and inversion-symmetry, but forbidden by TRS, we find $\boldsymbol{P} \propto \boldsymbol{E} \times \boldsymbol{B}$, electrical polarization parallel to the Poynting vector. This second-order response is distinct from the circular photogalvanic effect [28, 29], which only manifests in systems with broken inversion symmetry, and should therefore be absent in our system. The combination of these two responses therefore serve as a probe of the scalar TRS breaking.

A natural further question is, what is the classification of isotropic three-dimensional media with or without inversion symmetry in the other Altland-Zirnbauer symmetry classes [30]. The topological invariants outlined in this work remain valid if we also include TRS besides isotropy and inversion symmetry. Our models are compatible with prescribing TRS with the usual representation $\mathcal{T} = \exp(i\pi S_y)\mathcal{K}$, which fixes some parameters, but does not forbid any topological phases. In this case odd values of C_M correspond to an amorphous strong topological insulator [31], however, the gapless surface Dirac cones remain protected by mirror symmetry for even values as well. To our knowledge, TRS does not enrich the classification in the presence of isotropy and inversion symmetry; and the classification with isotropy, broken inversion and unbroken TRS is the same as the strong $\mathbb{Z}_2$ classification with TRS only. There is, however an interesting possibility that isotropy and the protection of the surface density of states in a doubled phase prevents the surface conductivity from going below the metal-insulator critical point, and because of that guaranteeing that the surface stays metallic. We leave an investigation of these properties to future work.

Our microscopic model—relying on orbital-selective hoppings through chiral magnetic molecules—demonstrates the difficulty of constructing a time-reversal odd, inversion even, scalar order parameter. In our case the order parameter is $\boldsymbol{P} \cdot (\boldsymbol{\nabla} \times \boldsymbol{M})$, electric polarization times bound current. Analyzing an effective field-theory displaying such order paramater without other symmetry breaking would shed further light on the properties of this class of isotropic magnetic materials.

Data availability

The data shown in the figures is available at [32].

Code availability

The code generating all of the data shown in the figures is available at [32].

Author contributions

D. V. proposed the initial project idea, all authors contributed to creating the research plan and later refining it. D. V. formulated the bulk invariants. A. A. and D. V. devised the microscopic system and the scalar time-reversal breaking mechanism. D. V. wrote the code generating amorphous structures and computing the spectral functions. A. A. wrote the code for constructing and solving the network models. H. S. performed the numerical simulations and wrote the manuscript with input from all authors. A. A. managed the project with input from all authors.

Acknowledgments

D. V. thanks Roderich Moessner for useful discussions. A. A. is grateful to Piet Brouwer for enlightening comments. The authors thank Elizabeth Dresselhaus and Bjorn Sbierski for sharing their network model code. The authors thank Isidora Araya Day for helping to set up and perform Pymablock calculations. A. A. and H. S. were supported by NWO VIDI grant 016.Vidi.189.180 and by the Netherlands Organization for Scientific Research (NWO/OCW) as part of the Frontiers of Nanoscience program. D. V. was supported by the Swedish Research Council (VR), the Knut and Alice Wallenberg Foundation, the Deutsche Forschungsgemeinschaft (DFG, German Research Foundation) under Germany's Excellence Strategy through the Würzburg-Dresden Cluster of Excellence on Complexity and Topology in Quantum Matter – ct.qmat (EXC 2147, project-id 57002544), and the National Research, Development and Innovation Office of Hungary under OTKA grant no. FK 146499.

References

[1] L. Šmejkal and T. Jungwirth, *Symmetry and Topology in Antiferromagnetic Spintronics*, pp. 267–298, Springer International Publishing, ISBN 978-3-319-97334-0, doi:10.1007/978-3-319-97334-0_9 (2018).

[2] L. Šmejkal, J. Sinova and T. Jungwirth, *Emerging research landscape of altermagnetism*, Phys. Rev. X **12**, 040501 (2022), doi:10.1103/PhysRevX.12.040501.

[3] L. Fu, *Topological crystalline insulators*, Phys. Rev. Lett. **106**, 106802 (2011), doi:10.1103/PhysRevLett.106.106802.

[4] A. Lau and C. Ortix, *Novel topological insulators from crystalline symmetries.*, Eur. Phys. J. Spec. Top. **227**, 1309 (2018), doi:10.1140/epjst/e2018-800098-y.

[5] K. Shiozaki and M. Sato, *Topology of crystalline insulators and superconductors*, Phys. Rev. B **90**, 165114 (2014), doi:10.1103/PhysRevB.90.165114.

[6] D. Varjas, A. Lau, K. Pöyhönen, A. R. Akhmerov, D. I. Pikulin and I. C. Fulga, *Topological phases without crystalline counterparts*, Phys. Rev. Lett. **123**, 196401 (2019), doi:10.1103/PhysRevLett.123.196401.

[7] Z. Ringel, Y. E. Kraus and A. Stern, *Strong side of weak topological insulators*, Phys. Rev. B **86**, 045102 (2012), doi:10.1103/PhysRevB.86.045102.

[8] L. Fu and C. L. Kane, *Topology, delocalization via average symmetry and the symplectic anderson transition*, Phys. Rev. Lett. **109**, 246605 (2012), doi:10.1103/PhysRevLett.109.246605.

[9] I. C. Fulga, B. van Heck, J. M. Edge and A. R. Akhmerov, *Statistical topological insulators*, Phys. Rev. B **89**, 155424 (2014), doi:10.1103/PhysRevB.89.155424.

[10] H. Spring, A. Akhmerov and D. Varjas, *Amorphous topological phases protected by continuous rotation symmetry*, SciPost Physics **11**(2) (2021), doi:10.21468/scipostphys.11.2.022.

[11] D. Varjas, T. Ö. Rosdahl and A. R. Akhmerov, *Qsymm: Algorithmic symmetry finding and symmetric Hamiltonian generation*, New J. Phys. **20**(9), 093026 (2018), doi:10.1088/1367-2630/aadf67.

[12] I. Araya Day, S. Miles, H. K. Kerstens, D. Varjas and A. R. Akhmerov, *Pymablock: an algorithm and a package for quasi-degenerate perturbation theory*, doi:10.48550/arXiv.2404.03728 (2024), `2404.03728`.

[13] Q. Marsal, D. Varjas and A. G. Grushin, *Topological weaire–thorpe models of amorphous matter*, Proceedings of the National Academy of Sciences **117**(48), 30260 (2020), doi:10.1073/pnas.2007384117.

[14] Z. Wang and B. Yang, *Topological hamiltonian as an exact tool for topological invariants*, J. Phys.: Condens. Matter **25**(155601) (2013), doi:10.1088/0953-8984/25/15/155601.

[15] A. Weiße, G. Wellein, A. Alvermann and H. Fehske, *The kernel polynomial method*, Rev. Mod. Phys. **78**, 275 (2006), doi:10.1103/RevModPhys.78.275.

[16] D. Varjas, M. Fruchart, A. R. Akhmerov and P. M. Perez-Piskunow, *Computation of topological phase diagram of disordered* $\mathrm{pb}_{1-x}\mathrm{sn}_x\mathrm{Te}$ *using the kernel polynomial method*, Phys. Rev. Res. **2**, 013229 (2020), doi:10.1103/PhysRevResearch.2.013229.

[17] D. K. K. Lee and J. T. Chalker, *Unified model for two localization problems: Electron states in spin-degenerate landau levels and in a random magnetic field*, Physical Review Letters **72**(10), 1510 (1994), doi:10.1103/physrevlett.72.1510.

[18] M. R. Zirnbauer, *Toward a theory of the integer quantum hall transition: Continuum limit of the chalker–coddington model*, Journal of Mathematical Physics **38**(4), 2007 (1997), doi:10.1063/1.531921.

[19] J. T. Chalker and P. D. Coddington, *Percolation, quantum tunnelling and the integer hall effect*, Journal of Physics C: Solid State Physics **21**(14), 2665 (1988), doi:10.1088/0022-3719/21/14/008.

[20] F. Evers and A. D. Mirlin, *Anderson transitions*, Reviews of Modern Physics **80**(4), 1355 (2008), doi:10.1103/revmodphys.80.1355.

[21] R. E. Miles, *Random polygons determined by random lines on a plane*, Proc. Natl. Acad. Sci. U.S.A. **52**(4), 901 (1964), doi:10.1073/pnas.52.4.901.

[22] D. Sanz-Hernández, A. Hierro-Rodriguez, C. Donnelly, J. Pablo-Navarro, A. Sorrentino, E. Pereiro, C. Magén, S. McVitie, J. M. de Teresa, S. Ferrer *et al.*, *Artificial double-helix for geometrical control of magnetic chirality*, ACS nano **14**(7), 8084 (2020).

[23] S. Ferlay, T. Mallah, R. Ouahes, P. Veillet and M. Verdaguer, *A room-temperature organometallic magnet based on prussian blue*, Nature **378**(6558), 701 (1995).

[24] M. Zentkova and M. Mihalik, *The effect of pressure on magnetic properties of prussian blue analogues*, Crystals **9**(2), 112 (2019).

[25] N. Ma, R. Ohtani, H. M. Le, S. S. Sørensen, R. Ishikawa, S. Kawata, S. Bureekaew, S. Kosasang, Y. Kawazoe, K. Ohara *et al.*, *Exploration of glassy state in prussian blue analogues*, Nature communications **13**(1), 4023 (2022).

[26] J. Bartolomé, E. Bartolomé, F. Luis, E. Burzurí, A. Camón, G. Filoti, A. M. Ako, J. Braun, V. Mereacre, C. E. Anson *et al.*, *Single-molecule magnet behavior and spin structure of an feiii7 cartwheel cluster revealed by sub-kelvin magnetometry and m ossbauer spectroscopy: The final pieces of the puzzle*, Inorganic Chemistry (2024).

[27] X. Yin, L. Deng, L. Ruan, Y. Wu, F. Luo, G. Qin, X. Han and X. Zhang, *Recent progress for single-molecule magnets based on rare earth elements*, Materials **16**(9), 3568 (2023).

[28] F. de Juan, A. G. Grushin, T. Morimoto and J. E. Moore, *Quantized circular photogalvanic effect in Weyl semimetals*, Nature Communications **8**, 15995 (2017), doi:10.1038/ncomms15995, `1611.05887`.

[29] F. Flicker, F. de Juan, B. Bradlyn, T. Morimoto, M. G. Vergniory and A. G. Grushin, *Chiral optical response of multifold fermions*, Phys. Rev. B **98**, 155145 (2018), doi:10.1103/PhysRevB.98.155145.

[30] A. Altland and M. R. Zirnbauer, *Nonstandard symmetry classes in mesoscopic normal-superconducting hybrid structures*, Phys. Rev. B **55**, 1142 (1997), doi:10.1103/PhysRevB.55.1142.

[31] A. Agarwala and V. B. Shenoy, *Topological insulators in amorphous systems*, Phys. Rev. Lett. **118**, 236402 (2017), doi:10.1103/PhysRevLett.118.236402.

[32] H. Spring, D. Varjas and A. R. Akhmerov, *Isotropic 3D topological phases with broken time- reversal symmetry*, doi:10.5281/zenodo.8212020, This work was supported by NWO VIDI grant 016.Vidi.189.180 (2023).

[33] C. W. Groth, M. Wimmer, A. R. Akhmerov and X. Waintal, *Kwant: a software package for quantum transport*, New Journal of Physics **16**(6), 063065 (2014), doi:10.1088/1367-2630/16/6/063065.

[34] P. Corbae, S. Ciocys, D. Varjas, E. Kennedy, S. Zeltmann, M. Molina-Ruiz, S. M. Griffin, C. Jozwiak, Z. Chen, L.-W. Wang, A. M. Minor, M. Scott *et al.*, *Observation of spin-momentum locked surface states in amorphous Bi_2Se_3*, Nature Materials **22**(2), 200 (2023), doi:10.1038/s41563-022-01458-0, `1910.13412`.

[35] H. C. Po, A. Vishwanath and H. Watanabe, *Symmetry-based indicators of band topology in the 230 space groups*, Nature Communications **8**(1) (2017), doi:10.1038/s41467-017-00133-2.

[36] B. Bradlyn, L. Elcoro, J. Cano, M. G. Vergniory, Z. Wang, C. Felser, M. I. Aroyo and B. A. Bernevig, *Topological quantum chemistry*, Nature **547**(7663), 298 (2017), doi:10.1038/nature23268, `1703.02050`.

[37] T. Van Mechelen and Z. Jacob, *Quantum gyroelectric effect: Photon spin-1 quantization in continuum topological bosonic phases*, Phys. Rev. A **98**, 023842 (2018), doi:10.1103/PhysRevA.98.023842.

A Model Hamiltonians

We use Qsymm to generate 3D class A models that respect inversion symmetry and isotropic continuous rotation symmetry, whose symmetry representations are:

$$U_{\mathcal{I}} = \sigma_0\tau_z,\ S_x = \frac{1}{2}\sigma_x\tau_0,\ S_y = \frac{1}{2}\sigma_y\tau_0,\ S_z = \frac{1}{2}\sigma_z\tau_0, \tag{A.1}$$

where $U_{\mathcal{I}}$ is the unitary part of the inversion operator, $S_{x,y,z}$ are the generators of continuous spin rotations around the x, y, and z axes, and the unitary part of the corresponding rotation operator is given by $U = \exp(i\boldsymbol{n}\cdot\boldsymbol{S})$ with $\boldsymbol{n}$ the axis and angle of rotation, and τ, σ are the Pauli matrices. τ represents the orbital component, and σ the spin component of the Hilbert space. The resulting model also has reflection symmetry on any 2D plane,

$$U_{\mathcal{M}_x} = i\sigma_x\tau_z,\ U_{\mathcal{M}_y} = i\sigma_y\tau_z,\ U_{\mathcal{M}_z} = i\sigma_z\tau_z, \tag{A.2}$$

where $U_{\mathcal{M}_{x,y,z}}$ is the unitary part of the reflection operators on the planes perpendicular to the x, y and z axes, or in general,

$$U_{\mathcal{M}_{\hat{\boldsymbol{n}}}} = \exp(i\pi\hat{\boldsymbol{n}}\cdot\boldsymbol{S})\tau_z, \tag{A.3}$$

where $\hat{\boldsymbol{n}}$ is a unit vector defining the mirror normal. Because of the full rotation invariance, prescribing one mirror symmetry results in mirror symmetry with respect to any plane.

The generated k-space model is listed in the main text in Eq. (1). In real-space, the model is of the form:

$$H^{\text{onsite}}_{4\times4} = \mu_1\sigma_0(\tau_0+\tau_z)/2 + \mu_2\sigma_0(\tau_0-\tau_z)/2, \tag{A.4}$$

$$\begin{aligned} H^{\text{hopping}}_{4\times4}(\boldsymbol{d}) &= (tn_1 + t_2 d^2)\sigma_0(\tau_0+\tau_z)/2 + (tn_2 + t_3 d^2)\sigma_0(\tau_0-\tau_z)/2 \\ &\quad + (t_0 - t_5 d^2)\boldsymbol{\sigma}\cdot\boldsymbol{d}\tau_y + (t_1 + t_4 d^2)\boldsymbol{\sigma}\cdot\boldsymbol{d}\tau_x, \end{aligned} \tag{A.5}$$

where tn_i are normal hopping terms, $\boldsymbol{d} = (d_x, d_y, d_z)$, with d_i the bond lengths along axis $i \in \{x, y, z\}$ that connect neighboring sites, and $d^2 = \boldsymbol{d}\cdot\boldsymbol{d}$.

When demonstrating that symmetry-breaking gaps out the surface Dirac-nodes, we introduce a mass term that breaks all symmetries except for continuous rotation around the x axis:

$$\lambda = (\sigma_0 + \sigma_x)\tau_y. \tag{A.6}$$

We also construct a doubled model. In k-space, this model takes the form:

$$\begin{aligned}H_{8\times8}(\boldsymbol{k}) &= 1/2(\rho_0+\rho_z)\sigma_0(\mu_1(\tau_0+\tau_z)/2+\mu_2(\tau_0-\tau_z)/2)\\&+1/2(\rho_0-\rho_z)\sigma_0(\mu_3(t\tau_0+\tau_z)/2+\mu_4(\tau_0-\tau_z)/2)\\&+(t_0(\rho_0+\rho_z)/2+t_3(\rho_0-\rho_z)/2)\boldsymbol{\sigma}\cdot\boldsymbol{k}\tau_x\\&-(t_4(\rho_0+\rho_z)/2+t_7(\rho_0-\rho_z)/2)\boldsymbol{\sigma}\cdot\boldsymbol{k}\tau_y\\&+(t_1+it_5)\rho_-\boldsymbol{\sigma}\cdot\boldsymbol{k}\tau_-+(t_1-it_5)\rho_+(\boldsymbol{\sigma}\cdot\boldsymbol{k}\tau_-)^\dagger\\&+(t_2+it_6)\rho_-\boldsymbol{\sigma}\cdot\boldsymbol{k}\tau_++(t_2-it_6)\rho_+(\boldsymbol{\sigma}\cdot\boldsymbol{k}\tau_+)^\dagger,\end{aligned} \tag{A.7}$$

where μ_i are chemical potential terms, t_i are the hopping terms, ρ, σ and τ are the Pauli matrices, $\boldsymbol{k}=(k_x,k_y,k_z)$, and $k^2=\boldsymbol{k}\cdot\boldsymbol{k}$. In real space, the model takes the form:

$$\begin{aligned}H_{8\times8}^{\text{onsite}} &= 1/2(\rho_0+\rho_z)\sigma_0(\mu_1(\tau_0+\tau_z)/2+\mu_2(\tau_0-\tau_z)/2),\\&+1/2(\rho_0-\rho_z)\sigma_0(\mu_3(\tau_0+\tau_z)/2+\mu_4(\tau_0-\tau_z)/2)\\H_{8\times8}^{\text{hopping}}(\boldsymbol{d}) &= 1/2(\rho_0+\rho_z)\sigma_0(tn_1(\tau_0+\tau_z)/2+tn_2(\tau_0-\tau_z)/2)\\&+1/2(\rho_0-\rho_z)\sigma_0(tn_3(\tau_0+\tau_z)/2+tn_4(\tau_0-\tau_z)/2)\\&+(it_0(\rho_0+\rho_z)/2+it_3(\rho_0-\rho_z)/2)\boldsymbol{\sigma}\cdot\boldsymbol{d}\tau_x\\&-(it_4(\rho_0+\rho_z)/2+it_7(\rho_0-\rho_z)/2)\boldsymbol{\sigma}\cdot\boldsymbol{d}\tau_y\\&+(-t_5+it_2)\rho_-\boldsymbol{\sigma}\cdot\boldsymbol{d}\tau_-+(t_5+it_2)\rho_+(\boldsymbol{\sigma}\cdot\boldsymbol{d}\tau_-)^\dagger\\&+(-t_6+it_1)\rho_-\boldsymbol{\sigma}\cdot\boldsymbol{d}\tau_++(t_2+it_6)\rho_+(\boldsymbol{\sigma}\cdot\boldsymbol{d}\tau_+)^\dagger,\end{aligned} \tag{A.8}$$

where tn_i are normal hopping terms, $\boldsymbol{d}=(d_x,d_y,d_z)$, with d_i the bond lengths along axis $i\in\{x,y,z\}$ that connect neighboring sites, and $d^2=\boldsymbol{d}\cdot\boldsymbol{d}$. The symmetry-breaking term for the doubled model is

$$\lambda'=\begin{pmatrix}1&1\\1&1\end{pmatrix}\otimes\begin{pmatrix}1&1\\1&1\end{pmatrix}\otimes\tau_y. \tag{A.9}$$

B Model and plotting parameters

In this section additional details of the plots are listed in order of appearance.

For panel (c) of Fig. 1 the Hamiltonian (D.1) was simulated using kwant [33] on a translationally invariant 3D face-centered cubic (FCC) lattice. Its eigenvalues were obtained along the high-symmetry points of the FCC lattice, using the parameters $\mu_1=0.1$, $\mu_2=0.2$, $t_1=0.3$, $t_2=-0.4$, $t_3=\exp(0.3i)$, $t_4=0.2i\exp(0.3i)$. For the dispersion shown in panel (d), a slab was simulated, periodic along the vectors $[1,0,0]$ and $[0,1,0]$, and with a width of 20 sites in the $[0,0,1]$ direction. The parameters used are the same as for panel (c).

For panel (a) of Fig. 3, the Chalker-Coddington network is composed of four unit cells in both x and y. For panel (b), the amorphous network was created with an outer radius of $R=20$, an inner radius of $r=4$, and a density of 1. The positions of the nodes of the network underwent a relaxation step where the position of each node is sequentially averaged over the position of all neighboring nodes. For panel (d), the results for single-mode Chalker-Coddington network were obtained for 249 different random scattering matrix configurations, for network sizes of 36, 72, 144, 288, 576, 1152, 2304 and 4608 unit cells, with an aspect ratio of 1. The results for the two-mode Chalker-Coddington network were obtained for the same network sizes and aspect ratio, and for 269 different scattering matrix configurations. For the amorphous network, the results were obtained for 50 outer radii sizes between $10^{1.5}$ and $10^{2.5}$, with a fixed outer radius over inner radius ratio of 1.5, and a density of 0.7. Results for the single mode network were obtained for 500 different amorphous network and scattering matrix configurations, and 300 different configurations for the two-mode amorphous network. Additional results for the single mode network were obtained for 5 outer radii sizes between $10^{2.5}$ and 10^3, for 100 different network configurations and scattering matrices.

For Fig. 2(a), single-Dirac cone model as defined in Eq. (A.4) was used. Its parameters were set to $\mu_1 = -1,\ \mu_2 = 1,\ tn_1 = 0,\ tn_2 = 0,\ t_0 = 0.5,\ t_1 = 0.4,\ t_2 = 1,\ t_3 = -1,\ t_4 = 0.3,\ t_5 = 0.8$ and the additional symmetry-breaking term λ from Eq. (A.6) is set to 0. For panels (b) and (d) the same model as panel (a) was used. Its parameters were set to $\mu_1 = 1,\ \mu_2 = -1,\ tn_1 = -2,\ tn_2 = 2,\ t_0 = 1,\ t_1 = 1,\ t_2 = 1.1,\ t_3 = 1.2,\ t_4 = 1.3,\ t_5 = 1.25$ and the additional symmetry-breaking term λ from Eq. (A.6) is set to 0. The results were obtained obtained for k-points between $-\pi$ and π. For panel (d) and (e), λ is set to 0.3. For the doubled model as defined in Eq. (A.8), the parameters were set to $\mu_1 = 1,\ \mu_2 = -1,\ \mu_3 = 1,\ \mu_4 = -1,\ tn_1 = -2,\ tn_2 = 2,\ tn_3 = -2,\ tn_4 = 2,\ \lambda_1 = 0.1,\ \lambda = 0.11,\ \lambda_3 = 0.12,\ \lambda_4 = 0.123$. The amorphous slab was generated in a box of dimensions $200 \times 50 \times 50$ and density 0.4.

For panel (a) of Fig. E.1, the model (A.4) was used. For all results, the hopping parameters were set to $t_0 = 1,\ t_1 = 1.2,\ t_2 = 0,\ t_3 = 0,\ t_4 = 0,\ t_5 = 0,\ tn_1 = -2,\ tn_2 = 2$ (terms proportional to k to the power of 2 and higher are set to 0). Since the only hopping terms are linear in d, in order to ensure that TRS is broken for this model, a different distance dependence is given for the t_1 and t_2: $t_1 \exp(-0.3d)$ and $t_2 \exp(-d)$, where $d = \sqrt{d^2}$ is the bond length. The amorphous samples are all contained within a cube of 30 x 30 x 30 sites, with a density of 0.7, and the crystal samples are all 10 x 10 x 10 sites. For the invariant ν_M (6) the numerical integration over the Brillouin zone of the effective Hamiltonian was done over a grid of 15 x 15 points.

For panel (b) of Fig. E.1, the model (D.1) was used. The parameters were set to $t_1 = 0.3,\ t_2 = -0.4,\ t_3 = \exp(0.3i),\ t_4 = i\exp(0.3i)$. The Γ and X points of the model are $(0,0,0)$ and $(0,2\pi,0)$.

C Isotropy of the amorphous model

In this appendix we confirm that the amorphous tight-binding model produces an isotropic electronic structure up to random fluctuations. The underlying amorphous structure was obtained by the same method as in Ref. [34], where we also confirmed the isotropy of its two-point correlation function, hence here we focus only on the isotropy of the electronic spectral function.

We generated amorphous structures in a box of dimensions $50 \times 50 \times 50$ with density 0.4, and calculated the spectral function by sampling a ball of radius 20 in the middle of the sample, with an average $N = 13400$ lattice sites. Same as Fig. 2(a), single-Dirac cone model as defined in Eq. (A.4) was used with parameters set to $\mu_1 = -1,\ \mu_2 = 1,\ tn_1 = 0,\ tn_2 = 0,\ t_0 = 0.5,\ t_1 = 0.4,\ t_2 = 1,\ t_3 = -1,\ t_4 = 0.3,\ t_5 = 0.8$. For the rest of this analysis, we fixed $|\mathbf{k}| = 1$ in inverse length units, and took 500 samples for the spectral function $A(E, |\mathbf{k}| = 1)$ (with E sampled at 400 values) from the following three random ensembles:

- Fixed disorder realization, random $\mathbf{k}$ with $|\mathbf{k}| = 1$,
- Random disorder realization, fixed $\mathbf{k} = (0, 0, 1)$,
- Random disorder realization, random $\mathbf{k}$ with $|\mathbf{k}| = 1$.

We plot the resulting distributions of $A(E, |\mathbf{k}| = 1)$ in Fig. C.1 top panel. The expectation values of the three distributions are indistinguishable, as illustrated in Fig. C.1 middle panel. When comparing the standard deviations, we find that the case with fixed disorder realization has significantly lower variance, while the other two are very similar, see Fig. C.1 bottom panel. It is is expected that a fixed disorder realization results in lower variance, as the samples from nearby **k**-points are correlated, as illustrated in Fig. C.2. The relative fluctuation of the spectral function amplitude is in the range of $1 - 2\%$ in all cases, a value expected from statistical fluctuations in a finite sample of this size, scaling with $\sqrt{N}$.

We further compare the two cases with random disorder realizations, by calculating the statistical p-value and the Kolmogorov–Smirnov statistic D for every E, see Fig. C.3. These both measure the similarity of the random distributions given a finite sample, high p values and low D values indicate high similarity, with $p = 1$ and $D = 0$ corresponding to identical samples. We find that at most E values the distributions are sufficiently similar, and there are only a few outliers where we should reject the null hypothesis that the underlying distributions are identical with 95% confidence. Such outliers are, however, expected to occur in a set of 400 random distributions. Hence we conclude, that the electronic structures obtained in our numerics are isotropic up to random fluctuations.

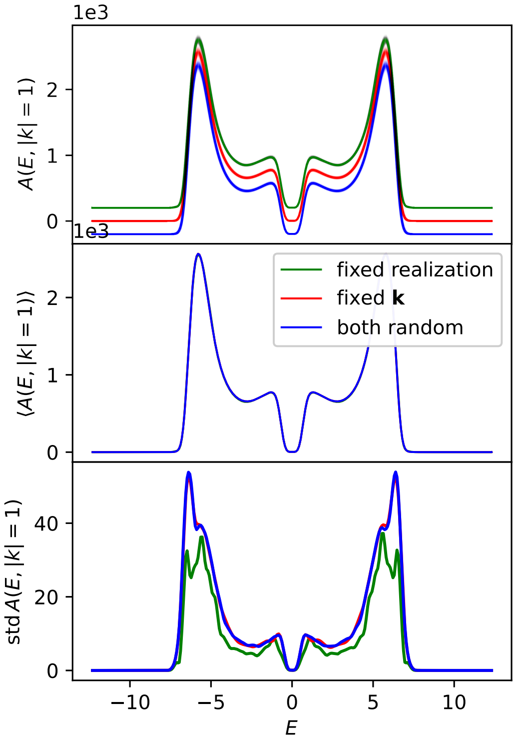

Figure C.1: Spectral function statistical properties of the amorphous model. Top panel: Probability density of the spectral function as the function of energy E at $|\mathbf{k}| = 1$ for three different ensembles. The plots are offset for visibility, and more saturated colors denote higher probability density. Middle panel: Expectation value of the spectral function. The three graphs completely overlap at this scale. Bottom panel: Standard deviation of the probability distributions.

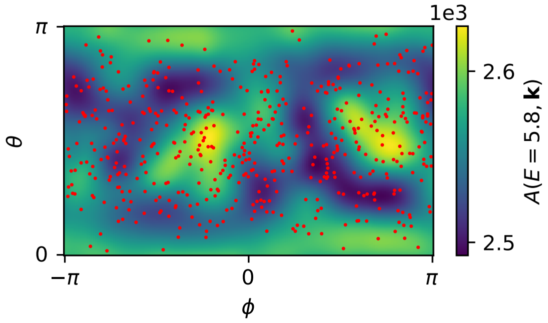

Figure C.2: Spectral function amplitude at $E = 5.8$ and $|\mathbf{k}| = 1$ for a fixed disorder realization as a function of the polar angles of $\mathbf{k}$. The results are interpolated, the red dots mark the sampled points.

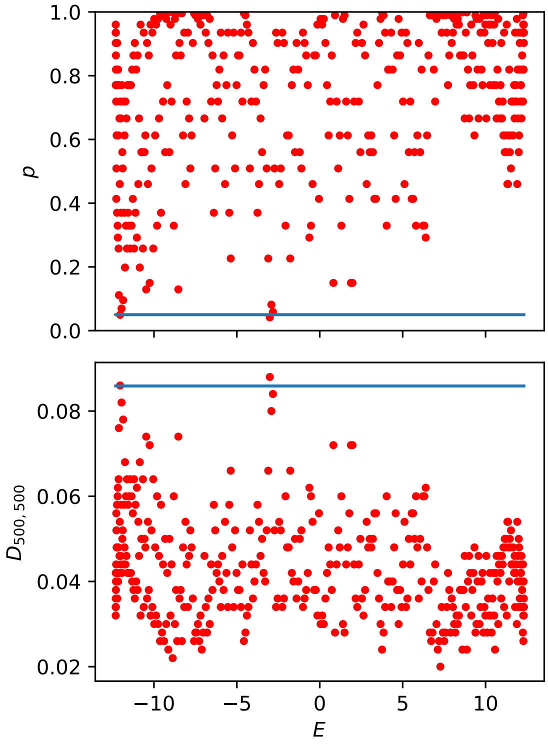

Figure C.3: Comparison of the probability distributions with random disorder realization with fixed or random $\mathbf{k}$. Top panel: statistical p values. The blue line denotes $p = 0.05$, for lower p the null hypothesis of the distributions being identical is rejected with 95% confidence. Bottom panel: Two-sample Kolmogorov–Smirnov statistic with 500 samples each. The blue line denotes the value over which the null hypothesis is rejected with 95% confidence.

D Spin splitting in a crystal

Because the scalar TRS breaking is insufficient to cause a spin splitting in an isotropic medium, we demonstrate the spin splitting in a crystal structure. We use the s and p atoms as the basis of the rock salt crystal structure [Fig. 1(b)] with full cubic (O_h) symmetry. In this model, orbitals of the same type are connected by normal hopping, and orbitals of different types are connected by the complex spin-orbit hopping of (4), resulting in terms off-diagonal in the orbital (τ) space. Because the symmetry-breaking mechanism relies on the nontrivial distance-dependence of the hopping phase, we include both nearest-neighbor as well as third-nearest-neighbor s–p hopping [Fig. 1(b)]. We emphasize that this is a minimal model used as a sanity-check, hence we ignore the problem with microscopic realization posed by the third-nearest-neighbour bonds crossing each other.

The tight-binding Hamiltonian thus takes the form:

$$\begin{aligned} H_{\text{salt}} = &\left(\mu_1 + t_1 \sum_{\boldsymbol{d}_2} e^{i\boldsymbol{k}\cdot\boldsymbol{d}_2}\right)\sigma_0(\tau_0+\tau_z)/2 + \left(\mu_2 + t_2 \sum_{\boldsymbol{d}_2} e^{i\boldsymbol{k}\cdot\boldsymbol{d}_2}\right)\sigma_0(\tau_0-\tau_z)/2 \\ &+ \frac{i}{a}\left(\sum_{\boldsymbol{d}_1} e^{i\boldsymbol{k}\cdot\boldsymbol{d}_1}\boldsymbol{d}_1\cdot\boldsymbol{\sigma}\right)(t_3\tau_+ + t_3^*\tau_-) + \frac{i}{a}\left(\sum_{\boldsymbol{d}_3} e^{i\boldsymbol{k}\cdot\boldsymbol{d}_3}\boldsymbol{d}_3\cdot\boldsymbol{\sigma}\right)(t_4\tau_+ + t_4^*\tau_-)\,, \end{aligned} \tag{D.1}$$

where a is the cubic cell lattice constant, $\sigma_\pm = \frac{1}{2}(\sigma_x \pm i\sigma_y)$, and similarly for $\tau_\pm$. $\boldsymbol{d}_1$ runs over the six nearest-neighbor bonds symmetry-equivalent to $\frac{a}{2}(1,0,0)$, $\boldsymbol{d}_2$ over the twelve next-nearest neighbor bonds symmetry-equivalent to $\frac{a}{2}(1,1,0)$, and $\boldsymbol{d}_3$ over the eight next-next-nearest neighbor bonds symmetry-equivalent to $\frac{a}{2}(1,1,1)$. The terms of Eq. (D.1) proportional to t_1 and t_2 are the next-nearest neighbor $s-s$ and $p-p$ normal hoppings respectively [dashed lines of Fig. 1(b)], where t_1 and t_2 are both real. The terms proportional to t_3 and t_4 are the nearest and next-next-nearest neighbor s–p hoppings respectively [solid lines of Fig. 1(b)], with t_3 and t_4 complex. This Bloch Hamiltonian reproduces the symmetry-allowed terms of the continuum model (1) in the long-wavelength limit, aside from an additional cubic anisotropy term and a slight change of parametrization.

The tight-binding model (D.1) preserves the space group of the rock salt crystal structure [see App. A]. The spin-orbit-like s–p hopping terms alternate in sign along the hopping axes in order to preserve inversion symmetry. We select the parameters $\mu_1 = 0.1,\ \mu_2 = 0.2,\ t_1 = 0.3,\ t_2 = -0.4,\ t_3 = \exp(0.3i),\ t_4 = 0.2i\exp(0.3i)$. The dispersion relation shows that the spin bands are split away from high-symmetry points and lines that have at least a rotation and a mirror symmetry, demonstrating that TRS is broken [Fig. 1(c)]. The TRS-breaking terms of our model are next-next-nearest neighbor terms, which leads to linear TRS-breaking terms intrinsically cancelling out and only cubic terms remaining. The surface dispersion shows gapless, propagating surface modes within the bulk gap [Fig. 1(d)].

E Alternative bulk invariants

In addition to the bulk invariant given in Sec. 2.2.1, we identify two alternative expressions.

E.1 Inversion eigenvalues

The inversion operator commutes with the spins at the rotation-invariant points $\boldsymbol{k} = \boldsymbol{0}$ and $\boldsymbol{k} = \infty$. Since the SU(2) rotation symmetry commutes with the inversion operator, the inversion eigenvalues come in degenerate pairs in the case of a spin-1/2 representation, and in degenerate groups of $2s+1$ for spin-s representations. The difference in parity of the inversion eigenvalue pairs at these rotation-invariant points characterizes the topological

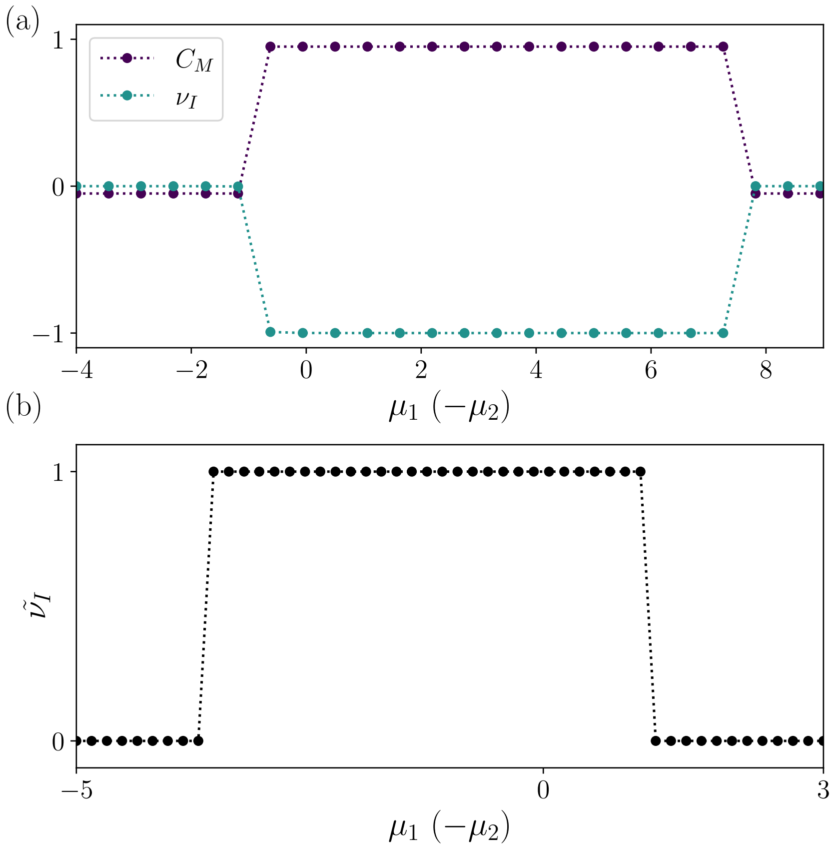

Figure E.1: Conductivity of translationally invariant and amorphous networks. (a) The topological invariants of the class A model (A.4) for amorphous systems (C_M defined in (6) and ν_I in (E.1)) as a function of chemical potentials $\mu_{1,2}$. Plots are offset for clarity. (b) The invariant $\tilde{\nu}_I$ of the crystal system as a function of chemical potentials $\mu_{1,2}$ (D.1). Plot details are in App. B.

phase:

$$\begin{aligned} \nu_I &= \frac{1}{2}\left[\iota_-(\infty) - \iota_-(\mathbf{0})\right], \\ \iota_-(\boldsymbol{k}) &= \mu_{-1}\left(\langle n(\boldsymbol{k})|\,\mathcal{I}\,|m(\boldsymbol{k})\rangle\right), \end{aligned} \tag{E.1}$$

where $|n(\boldsymbol{k})\rangle$ are the occupied states of the effective Hamiltonian H_{eff}, and $\mu_\lambda(A)$ indicates the multiplicity of the eigenvalue λ in the spectrum of A. We note that in the case of an operator that only has ± 1 eigenvalues, the multiplicity can be expressed through the trace as $\operatorname{Tr} A = N - 2\mu_{-1}(A)$, allowing to rewrite the invariant as

$$\nu_I = -\frac{1}{4}\sum_{n\in\text{occ}}\left(\langle n(\infty)|\,\mathcal{I}\,|n(\infty)\rangle - \langle n(\mathbf{0})|\,\mathcal{I}\,|n(\mathbf{0})\rangle\right), \tag{E.2}$$

where we used that the total number of occupied bands is the same at $\boldsymbol{k} = \mathbf{0}$ and ∞.

While we only consider spin-1/2 representations in the main text, in the general case it is possible to resolve the eigenstates at $\boldsymbol{k} = \mathbf{0}$ and ∞ based on the spin-representation $\boldsymbol{S}$. All states along a line $\hat{\boldsymbol{n}}k$ connecting $\mathbf{0}$ and ∞ have continuous rotation symmetry along the $\hat{\boldsymbol{n}}$ axis, hence the eigenvalues of $\hat{\boldsymbol{n}} \cdot \boldsymbol{S}$ in the occupied subspace are well-defined throughout, and the total number of various spin representations cannot change. The inversion eigenvalues, however, can change in the process, so we can define the set of invariants

$$\begin{aligned}\nu_I^s &= \frac{1}{2s+1}\left[\iota_-^s(\infty) - \iota_-^s(\mathbf{0})\right], \\ \iota_-^s(\boldsymbol{k}) &= \mu_{-1}\left(\langle n_s(\boldsymbol{k})|\,\mathcal{I}\,|m_s(\boldsymbol{k})\rangle\right),\end{aligned} \tag{E.3}$$

where we restrict the inversion operator to the subspace corresponding to the spin-s representation spanned by the states $|n_s(\boldsymbol{k})\rangle$. This results in a $\mathbb{Z}^{\mathbb{N}}$ classification, of which the invariant (E.1) only probes a $\mathbb{Z}$ subset,

$$\nu_I = \sum_s \left(s + \frac{1}{2}\right)\nu_I^s. \tag{E.4}$$

This relation also shows that, depending on the spin representation content of the model, not all values of ν_I may be realizable. A remaining question is, whether for general s, ν_I or the set of ν_I^s has a bulk-boundary correspondence in amorphous systems. As we show in the next section (see (E.9)), it is a different combination of ν_I^s that the mirror Chern invariant probes, nontrivial values of which we expect to protect robust surface states. The simplest continuum model with trivial ν_I (or C_M) and nontrivial ν_I^s has 16 on-site degrees of freedom (4 spin-1/2 and 2 spin-3/2 representations, half of which is inversion-odd), we leave analysis of the surface physics to future work.

For the crystalline system described in Sec. D we calculate the analogous eigenvalue parity invariant given by:

$$\tilde{\nu}_I = \frac{1}{2}\left[\iota_-(\Gamma) + \iota_-(X)\right] \mod 4, \tag{E.5}$$

where ι is the same as in (E.1). The mod 4 results from factoring out atomic insulators located at other Wyckoff positions. We note that (E.5) does not give the full symmetry indicator classification in space group 225 [35,36], and the $\mathbb{Z}$ invariant given by the mirror Chern number also remains well defined and contains additional information.

E.2 Rotation eigenvalues

Another way to formulate the bulk invariant relies on the Chern-number being expressible through the difference in the occupied rotation eigenvalues at the rotation-invariant points $\boldsymbol{k} = \mathbf{0}$ and $\boldsymbol{k} = \infty$ [13,37]:

$$C = \sum_{n\in\mathrm{occ}} \left(\langle n(\infty)|\,S_z\,|n(\infty)\rangle - \langle n(\mathbf{0})|\,S_z\,|n(\mathbf{0})\rangle\right), \tag{E.6}$$

where S_z is the generator of rotations around the z axis and the Chern-number is calculated in the $k_z = 0$ plane (other orientations give equivalent results). To formulate the mirror Chern number, we insert $-iM_z$, which adds a ±1 prefactor to the mirror-even/odd states:

$$C_M = -\frac{1}{2}\sum_{n\in\mathrm{occ}} \left(\langle n(\infty)|\,iM_zS_z\,|n(\infty)\rangle - \langle n(\mathbf{0})|\,iM_zS_z\,|n(\mathbf{0})\rangle\right). \tag{E.7}$$

In general $M_z = \mathcal{I}\exp(i\pi S_z)$, in the spin-1/2 case this simplifies to $M_z = i\mathcal{I}\sigma_z$, hence $-iM_zS_z = \frac{1}{2}\mathcal{I}$. Substituting this, we find

$$C_M = \frac{1}{4}\sum_{n\in\mathrm{occ}} \left(\langle n(\infty)|\,\mathcal{I}\,|n(\infty)\rangle - \langle n(\mathbf{0})|\,\mathcal{I}\,|n(\mathbf{0})\rangle\right) = -\nu_I. \tag{E.8}$$

For general spin, using that $\mathcal{I}$ commutes with the spin operators, after some algebra we find

$$\begin{aligned} C_M =& \frac{1}{4}\sum_s (-1)^{s-\frac{1}{2}} \sum_{n_s \in \mathrm{occ}_s} \left(\langle n_s(\infty)| \, \mathcal{I} \, |n_s(\infty)\rangle - \langle n_s(\mathbf{0})| \, \mathcal{I} \, |n_s(\mathbf{0})\rangle \right) \\ =& \sum_s (-1)^{s+\frac{1}{2}} \left(s + \frac{1}{2} \right) \nu_I^s . \end{aligned} \tag{E.9}$$

As we saw, in the spin-1/2 case studied in detail, Eqs. (6, (E.7), and (E.1)) are all equivalent formulations of the same invariant, as demonstrated by their equivalence for different values of the chemical potential [Fig. E.1(a)].

F Amorphous network model

In order to ensure four-fold coordination of each node of the amorphous network, we generate the network following the method described in Refs. [13, 21], which creates a graph by generating N random lines on a plane, with N chosen from a Poisson distribution whose mean is set to $2R\sqrt{\pi\rho}$, with ρ the chosen density of the graph and R the outer radius of the network. The angle and offset of the lines is uniformly distributed in $[0, 2\pi)$ and $[0, R]$ respectively. We define the intersections of each pair of lines as a network node. We ensure the two-in-two-out pattern of propagating modes at each node by orienting the links in an alternating fashion along each of the straight lines. There is no dependence of the scattering matrices on the length of the network links.

The graph is cut into an annulus shape by removing all of the nodes beyond the outer radius R and within the inner radius r. This ensures periodic boundary conditions along the polar angle coordinate. In order to maintain four-fold connectivity in the bulk of the graph, the nodes outside of the network that are connected to nodes inside of the network are changed into sinks or sources, that either absorb modes from the network or emit modes to the network. The conductivity of the amorphous network is calculated by $g = G\ln(R/r)/2\pi$, with $G = (e^2/h)\sum_{i,j}|S_{ij}|^2$, S_{ij} being the matrix element of the scattering matrix that connects the incoming modes originating from external sources beyond the network's outer edge to the outgoing modes exiting the network from its inner edge. A relaxation of the graph for visual clarity is optionally performed by averaging each node position to the center of its neighbors' positions.